

Dynamical models for sand ripples beneath surface waves

Ken Haste Andersen^{1,2,3}, Marie-Line Chabanol^{1,4}, Martin van Hecke^{1,5}

¹ Center for Chaos and Turbulence Studies, The Niels Bohr Institute, Blegdamsvej 17, 2100 Copenhagen Ø, Denmark.

² Institute of Hydraulic Research and Water Resources, the Technical University of Denmark, 2800 Lyngby, Denmark.

³ Dipartimento di Fisica, Universit degli Studi di Roma La Sapienza, Piazzale Aldo Moro 2, I-00185 Roma, Italy.

⁴ Institut Fourier, 100 rue des Mathématiques, Domaine Universitaire, 38400 Saint Martin d'Hères, France.

⁵ Max-Planck-Institut für Physik komplexer Systeme, Nöthnitzer Str. 38 01187 Dresden, Germany.

(December 2, 2024)

We discuss models for sand ripples under oscillatory flow. Our starting point is a detailed model of the turbulent fluid motion and the sand-water interaction. A numerical study of this model yields information on the mass transport between adjacent ripples as a function of their dimensions. Simpler models that account for conservation laws, symmetries and the mass transport obtained from the detailed model are then developed. We first study models for one-dimensional ripple patterns. A stability analysis reveals that ripple patterns possess short wavelength instabilities, both for ripples of too large and too small wavelengths. Dynamically, the final state occurs via the coarsening of initial small wavelength states; we study this process numerically and obtain a rather sharply “selected” final wavelength. The one-dimensional model is extended to describe two-dimensional patterns, and the dynamics of defects and the coarsening of the patterns is studied in this context.

45.70.Qj, 47.32.Cc, 47.27.Nz, 45.50.Jf

I. INTRODUCTION

A flat surface of sand, exposed to the flow of air or water, is almost never stable, but instead displays the formation of *patterns* [1–6]. Such pattern formation occurs on a variety of length-scales. Sand ripples have typical wavelengths on the order of centimeters, dunes are on the order of 10–100 meters, and, on the order of many kilometers, one finds the impressive draas of the desert or the sand waves in the sea [6].

This paper focuses on the so-called *vortex ripples* [1] which are created by oscillatory fluid flow, for instance beneath surface waves (see Fig. 1). Such ripples have attracted the attention from the coastal engineering community for a long time, since they are important for the sediment transport [7] and determine the bottom boundary condition for flow in the coastal region [8]. More recently vortex ripples have attracted the attention of physicists interested in non-equilibrium systems [4,9,10]; there is also a growing interest in related systems of wind-blown ripples [11–15] or ripples generated by steadily flowing fluids [2,16].

In this paper we introduce and discuss relatively simple models for the pattern formation in vortex ripples. In comparison to more traditional pattern forming systems, such as Rayleigh-Bénard convection or Faraday crispation [17], the underlying physics of sand ripples is very complicated. The fluid flow above fully developed ripples is in many cases turbulent, and the fluid vortices (see below) that drive the dynamics lead to non-local effects. The granular nature of the sand induces additional complications. The slopes of sand ripples have a maximal angle, the so-called angle of repose, which is essentially due to the avalanche properties of the sand. If one were



FIG. 1. Side-view of a vortex ripple pattern under oscillatory flow in a long, slender channel (courtesy of J.L. Hansen).

to develop a continuum description, this would induce a very “hard” nonlinearity.

The phenomenology of pattern formation in sand also suggest difficulties for modeling. Most noteworthy is the highly “subcritical” nature of the transition between a flat bed and a ripple state. Due to the friction between the sand grains, below a certain driving the sand-bed can freeze in any profile (provided that the local angles are below the angle of repose). As a consequence, once a ripple pattern is formed, it will simply remain when the driving by the fluid flow is turned off. It is amusing to note that for very hard driving the ripples disappear and the final state is a flat bed again. All in all, it is clear that the fully developed ripples are, in many aspects, very far away from onset, and that a description based on an expansion around the flat bed can not be expected to explain even qualitatively the fully developed state. For example, the wavelengths of the most unstable modes of a flat bed [18–20] are a factor ~ 4 smaller than the final wavelengths in fully developed ripples.

Due to the difficulties summed up above, our focus will not be on detailed modeling, but instead we propose simple models to capture the essential properties of ripple patterns. Our focus will be on the intermediate and late stages of ripple dynamics, and we will not be

interested in the initial stages of the growth of ripples from a flat bed. Symmetry arguments are an important ingredient in the construction of our models, but we complement those with a realistic law for the mass-transport between ripples. This law is based on extensive numerical simulations that we will discuss briefly in section II B (a more extensive account can be found in [21,22]). Additionally, our intuition is guided by experiments that are currently being performed in the Copenhagen group [4] (see Fig. 1). In this way we make a solid connection to the physics and go beyond a pure “toy”-model approach. Our discussion of the physics underlying ripple formation is given in section II. We start by giving a brief historic overview of earlier work on vortex ripples in section II A, and then discuss the results from detailed numerical investigations in section II B. The main result we want to focus on concerns the transport of sand between adjacent ripples. We then introduce and discuss simple one-dimensional models that are based on this transport in section III. In particular we study the coarsening process in these models that yields a rather sharply determined final wavelength in section III C. These models are extended to two-dimensional geometries in section IV, and we study the motion of defects and the wavelength evolution in section IV B. We close the paper by an discussion of results and outstanding questions.

II. VORTEX RIPPLES

Before focusing on the vortex ripples that occur under oscillatory fluid flow, we would like to outline the main differences between such vortex ripples on the one hand, and ripples under steady water flow (such as those found in river-beds) or aeolian ripples under a steady *air* flow on the other hand. First of all, ripples generated by a steady flow are asymmetrical and migrate. Vortex ripples under oscillatory flow are, on average, symmetrical and do not migrate. Secondly, the sand transport occurs by different mechanisms depending on whether the driving is done by air or by a fluid. In fluids, the density ratio s of the grains and the fluid is of order 1, and in this case the grains that participate in the transport are more or less following the flow of the water. In air, however, the density ratio s is of order 1000, and the sand transport mechanism is quite different. In this case one distinguishes between two types of sand motion. The grains that are scooped up from the bed by the wind and perform long jumps are called *saltating*. On the other hand, many grains on the surface of the bed perform only creep or *reptation*. This reptation, which is believed to be the key ingredient for the understanding of aeolian ripples [1,13,15], is driven by saltating grains impacting on the surface.

After this introduction, we will focus now exclusively on vortex ripples under oscillatory flow.

A. Historical overview

The oscillatory motion of water above a flat bed of sand can destabilize the sand surface and lead to the formation of ripples. The first to study the ensuing ripples was H. Ayrton [23] in 1910, and the subject was taken up again with the seminal work of Bagnold in 1946 [3]. In his studies, Bagnold distinguished between two kinds of ripples. Starting from an unstable flat bed, *rolling grain ripples* are formed [5]. They consist of small triangular ridges separated by a comparatively long stretch of flat bed. These ripples are unstable, and grow and coarsen to become *vortex ripples*, which are bigger and have essentially no flat bed between them. In this case the flow over the ripples generates *separation bubbles* (vortices) in the lee sides of the ripples.

Many experiments have been performed to study the vortex ripples since these early works. The focus has been on measuring the average wave length of the ripples [24–27], the friction and the roughness of the rippled bed [8,28–30], the dissipation of the surface waves by the ripples [31] or the sediment transport over ripples [7]. It was found that ripples form as soon as the fluid motion is strong enough to induce motion of the sand. For very hard driving, on the other hand, the sand is thrown into suspension and the ripples become shorter and more irregular, until they are finally washed away. We will concentrate on the intermediate regime, where the ripples are fully developed. In this regime the length of the ripples was found to be proportional to the amplitude of the oscillatory flow a , and to be roughly independent of the frequency. Estimates in the literature for the proportionality constant λ/a show a large spread, somewhere between 1 and 2, with a preference of values around 1.3 (see Fig. 8 in [25]).

Recently the ripples have also been studied from the view point of pattern formation. Both Scherer *et al.* [10] and Stegner and Wesfreid [9] studied a one-dimensional annular system to guarantee the conservation of sand. These experiments confirm that rolling grain ripples are essentially a transient that occurs on the way from a flat bed to the formation of vortex ripples. Stegner and Wesfreid [9] observed strong hysteresis when the driving amplitude of fully developed ripples was ramped up and down. When the amplitude of the driving was increased, the ripples became longer, but when it was decreased, the ripples did not change length. Scherer *et al.* [10] pointed out the coexistence of two different wavelengths when the frequency was high enough. Experiments on two-dimensional pattern formation performed by the Copenhagen group show interesting secondary instabilities, and in general a rich variety of patterns, including various types of defect motion [4].

On the theoretical side, Blondeaux and Vittori [18–20] have performed a linear and non-linear stability analysis of a flat bed. These works can only account for the

onset of ripple formation. Due to the difficulties mentioned above with the strong subcriticality and the large difference between the wavelengths of the first linearly unstable modes and the final patterns, this bears little or no relevance to fully developed vortex ripples. Most other theoretical work on ripples have focussed on the aeolian ripples, which are of little relevance here. A relatively unknown exception is the heuristic model for the shape of vortex ripples by Fredsøe and Brøker [32].

B. Numerical studies

Recently, one of us (KHA) has conducted a detailed numerical study of the vortex ripples [21,22], and we will discuss some of the main results below. We start by a discussion on the methods used to model the turbulent fluid motion and sediment transport. We then discuss qualitatively the formation of separation bubbles and their role in generating and maintaining the sand ripples. Based on the simulations, we have obtained, as a function of the ripple spacing, the transport of mass between ripples for states consisting of equal sized, fully developed ripples. This mass transport will play a crucial role in the models that we develop later on.

1. Detailed model

The computational model [21,22] consists of two parts: a flow model and a sediment transport model. The flow model calculates the flow over the ripples for a fixed ripple profile. From this flow, the shear stress on the bed is extracted and used to calculate the sediment transport in the so-called *bed load* layer.

a. Fluid flow. The dynamics is driven by an oscillatory forcing:

$$u(t) = a\omega \sin(\omega t), \quad (1)$$

where a denotes the amplitude of the fluid motion and ω its angular frequency; the fluid is furthermore characterized by its viscosity ν . Since the scale of the ripples is of order a , the relevant Reynolds number is of order $a^2\omega/\nu$, which for typical driving parameters in an experimental situation ($a=5$ cm, $\omega=3$ s $^{-1}$) and water is of order 10^3 ; the flow is clearly turbulent. The detailed modeling of the flow is based on a numerical calculation of the fully turbulent flow using the standard k - ω turbulence model [33]. The boundary conditions at the bottom are given by the shape of the ripples and the Nikuradse roughness length k_N (e.g. [34]) which characterizes the size of the grains.

Using a as the relevant length scale and characterizing the ripples by their dimensional lengths and heights λ_{dim} and h_{dim} we can use the following non-dimensional parameters:

$$\lambda = \frac{\lambda_{dim}}{a}, \quad h = \frac{h_{dim}}{a}, \quad Re = \frac{a^2\omega}{\nu}, \quad k_N = \frac{k_{N, dim}}{a}. \quad (2)$$

In a fully developed turbulent flow the large scale structures are independent of the Reynolds number. We therefore expect the separation bubbles created by the ripples and the shear stresses on the bed to be independent of the Reynolds number. The magnitude of the grain roughness is of minor importance as long as $k_N \ll 1$. We then see that the two dominant parameters characterizing the flow are the dimensions of the ripples λ and h . The fact that the frequency ω does not appear in the non-dimensionalization of the flow over the ripples, indicates that we can expect this parameter to be of minor importance for the final wavelength of the ripples. Note however, that even though qualitatively the fluid flow is essentially independent of ω , the mass transport will depend on the frequency (see below).

b. The sediment transport. The sediment transport is governed by the shear stress on the bed. The associated non-dimensional parameter is known as the *Shields parameter* and expresses the ratio between the drag and gravitational forces on a single grain (For an introduction to sediment transport see chapter 7 in ref. [34]):

$$\theta \equiv \frac{\tau}{\rho_w(s-1)gd}. \quad (3)$$

Here τ is the dimensional shear stress on the bed, ρ_w is the density of water, s is the ratio between the density of sand and water (a typical value for the water/quartz sand case is 2.65), g denotes gravity and d is the mean diameter of the grains.

The non-dimensional flux of sand ϕ in the bed load layer, the so-called bed load, is a function of the local Shields parameter, and can be modeled as:

$$\phi = \alpha(\theta - \theta_c)^\beta, \quad (4)$$

where θ_c is the critical value of the Shields parameter below which grains do not move. For turbulent boundary layers θ_c is approximately constant: $\theta_c \approx 0.05$ [34]. The constants α and β have been determined empirically by Meyer-Peter and Müller [35] to be approximately $\alpha=8$ and $\beta=1.5$, which are in good agreement with theoretical estimates of ϕ , (see [36,37]). The formation and the dynamics of the ripples is mainly determined by the fluid flow, and the exact values of the constants α and β and also the detailed form of Eq. (4) turn out to be relatively unimportant for the content of this work.

For strong flows or small grain diameter, sand will be thrown into suspension and be advected by the flow. In this case another parameter describing the amount of suspension enters, namely the settling velocity of the grains w_s . As sand can be transported over large distances in this case, the suspension can introduce interactions between ripples that are not adjacent and the ripple wavelengths can no longer be expected to be independent of

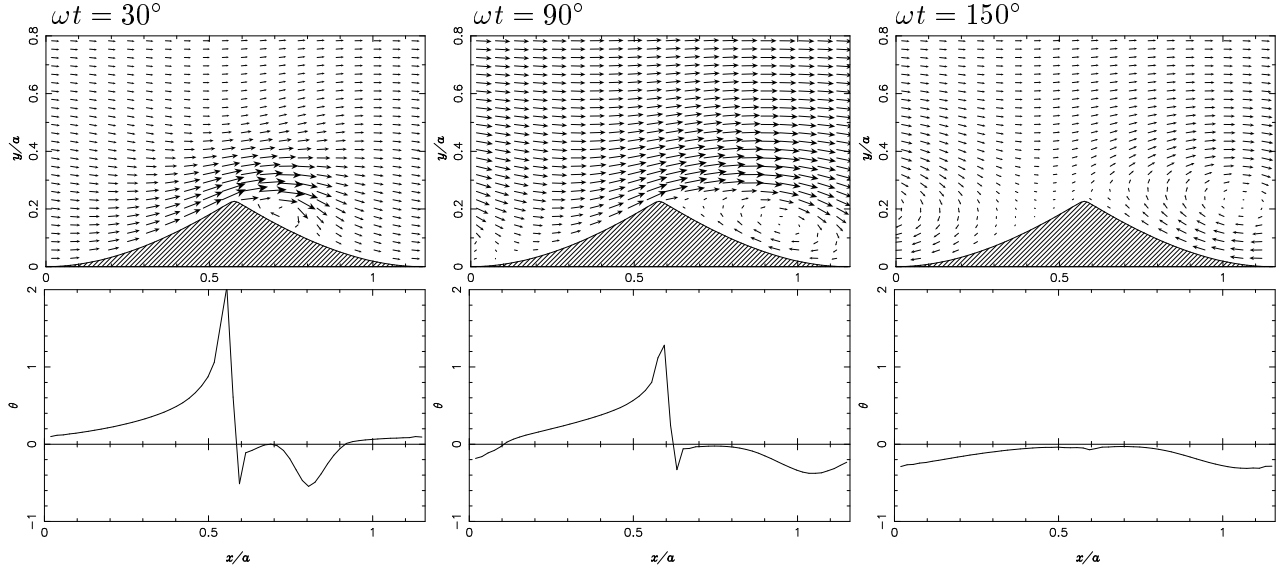


FIG. 2. The flow over a ripple at three instants in the first half of the wave period. The system consists of a single ripple in a system with periodic boundary conditions and length 1.15. The bottom three figures show the spatial profile of the Shields parameter on the bed at the corresponding times.

the frequency ω . In this work we assume to operate in a regime where the suspension is not important, so that the transport is only governed by the bed load.

2. Results from detailed numerical studies

In this section we will show some results on the detailed flow field and shear stress for fully developed vortex ripples. Most importantly, we characterize the transport of sand for a range of non-dimensional ripple lengths λ .

a. Flow structure. In Fig. 2 three snapshots for the flow over a fixed ripple of $\lambda = 1.15$ are shown. After a number of oscillations the flow equilibrates, and the first and second half of the oscillation (when the flow is, respectively, to the right and to the left) are related by symmetry; hence we only show the flow in the first wave period (at $\omega t = 30^\circ$, $\omega t = 90^\circ$ and $\omega t = 150^\circ$).

We see that there are two mechanisms at work that generate the shear stress at the bed. On the “wind”-side (which is here left), the converging flow yields uphill sediment transport. In the lee side of the ripple (to the right), a strong separation bubble is being created very early in the wave period ($\omega t = 30^\circ$). A separation bubble is an area where the flow near the bed reverses such that it is directed against the mean flow direction. The bubble moves out into the trough of the ripple ($\omega t = 90^\circ$), where it stays ($\omega t = 150^\circ$) until it is thrown over the crest as the flow reverses. The shear stress resulting from these processes is typically several times stronger than the stresses on a flat bed.

Clearly, the flow is uphill on both sides of the ripple, and consequently sand is transported from the trough

towards the crest. This is of course also the case in the other half period, and the net result is a steepening of the ripple profile. This steepening continues until the slopes of the ripple are at the angle of repose. Higher slopes are relaxed by avalanches, and in this way the area around the crest of the fully developed ripples have slopes close to the (dynamical) angle of repose. This is also evident from experiments [9].

b. Mass transport. The ripples interact by exchanging sand over the troughs. The amount of this mass flow is closely connected to the extension and strength of the separation bubble. Since its size will be roughly determined by the amplitude of the oscillations a , we can study the mass transport by taking a periodic set of ripples for various values of λ . This is illustrated in Fig. 3 where we show the total sediment transport during the first half wave period, for short ($\lambda = 0.6$), medium ($\lambda = 1.15$) and large ripples ($\lambda = 2.0$). For short ripples the separation bubble almost covers the whole space between the two ripple maxima, but is not very strong. For long ripples, on the other hand, the separation bubble does not reach over the trough, and therefore there is little or no mass flow between adjacent ripples. The most mass is exchanged for medium sized ripples, where the separation bubble is both strong and reaches over the trough.

We define \tilde{f} as the amount of sand transported over the trough during the first half wave period:

$$\tilde{f}(\lambda) = - \int_0^{\pi/\omega} \phi(x_{tr}, t) dt, \quad (5)$$

where x_{tr} is the position of the trough. Note the minus sign, which makes $\tilde{f}(\lambda)$ positive; this simplifies notation

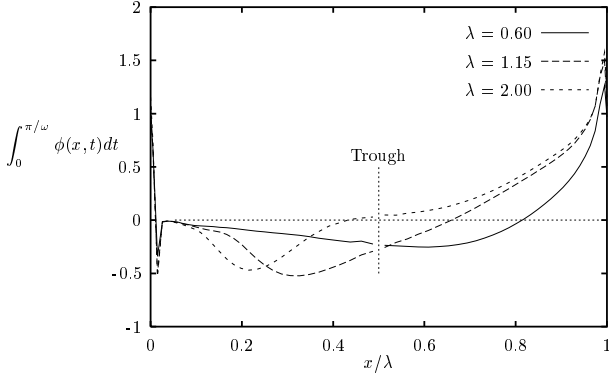


FIG. 3. The spatial profile of the mass transport averaged over the first half of the wave period ($\int_0^{\pi/\omega} \phi(x, t) dt$) for ripples of length $\lambda = 0.6, 1.15$ and 2.0 . Note that the ripple trough is located in the middle of the figure.

later on. This sign is simply related to the fact that the fluid and mass flows have opposite direction during each half period. Later on, we will also define the mass transport as a function of the length of the *side* of the ripple; we will denote this quantity by f : $f(z) = \tilde{f}(2z)$.

The function $\tilde{f}(\lambda)$ is shown in Fig. 4. This calculation was performed for a single ripple with periodic boundaries, for two different values of the steepness h/λ . In both cases \tilde{f} has a maximum around $\lambda \approx 1$, so ripples of this length have the largest exchange of sand.

III. DISCRETE MODELS FOR ONE-DIMENSIONAL RIPPLES

In this section we will introduce and study two simple models for ripples in a one-dimensional geometry. The models are intended to describe well-developed vortex ripples; in particular the early stages of the formation of ripples from a flat bed will be outside their scope. In spirit, our models are much closer to phase equations than to amplitude equations [17].

For simplicity it is assumed that the slopes of the ripples in our models are fixed at a certain angle (as in Figs. 5 and 6). The only degrees of freedom left then are the positions of the crests and the troughs of the ripples, or equivalently, the lengths of the ripples. This assumption reflects the observation that the slopes of ripples in experiments are close the angle of repose, and that the essential parameter for ripples is their dimension; all details of the ripple shape are deemed unimportant.

The dynamics of the ripple patterns are invariant with respect to translational symmetries, and with respect to a gauging of the height of the ripple profile. These symmetries are accounted for when the ripples are parameterized by their lateral dimensions λ (as in Fig. 5) or l and r (as in Fig. 6). We will assume our models to have periodic boundary conditions, and so the models have to

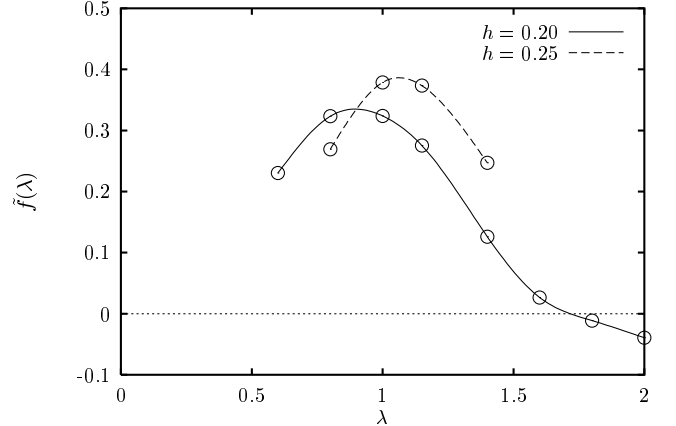


FIG. 4. The bed load in the trough averaged over one half wave period for two different values of the steepness as a function of the ripple length. The curves interpolating between the points are drawn using cubic splines.

satisfy a conservation of length. This conservation law and the conservation of sand-mass will be discussed below.

Our models incorporate the physics via the mass transfer function $\tilde{f}(\lambda)$. The mass transfer function has been determined for ripples of equal size, and to be able to describe more general patterns, we have to make some assumption for the mass transport between ripples of unequal size; this will be described in section III A below.

Two different models will be described. In the simplest case we characterize each ripple by their length only, and ignore as many details as possible; the ensuing “minimal model” is formulated in section III A. We refine this model in section III B and the outcome of our analysis of the latter model is discussed in section III C.

A. Minimal model

In this model, the basic building blocks are triangular and symmetric ripples with a given length λ_i . Suppose we want to determine the mass transfer between two ripples with lengths λ_1 and λ_2 (Fig. 5). We want to use the information that we have for the mass transfer between equal ripples. When λ_1 and λ_2 are approximately equal, one expects the size and strength of the separation bubble emanating from the crest of ripple 1 to depend mainly on the size of this ripple; the size of the adjacent ripple 2 will only be of minor importance. This leads to our central assumption: *the mass transport during a half period only depends on the size of the ripple that creates the separation bubble*. We expect strong deviations from this assumption only for neighboring ripples of very different size; our models are however intended to describe near-homogeneous situations.

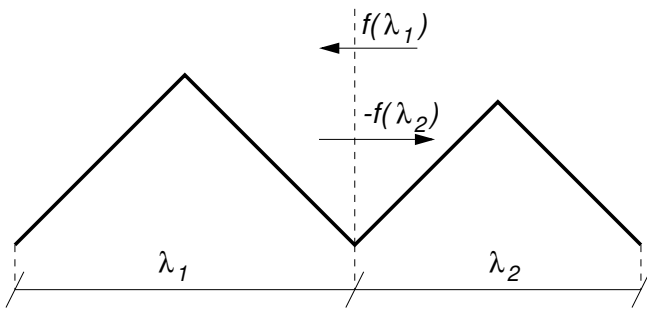


FIG. 5. An example of how the transport in the trough between two ripples is constructed as the transport in the two half periods.

Let us denote the first half period of the driving, when the flow is from left to right, by a subscript I , and the second half by II . Under the assumption stated above, we obtain: $\Delta m_I = \tilde{f}(\lambda_1)$ and $\Delta m_{II} = -\tilde{f}(\lambda_2)$, where Δm_I denotes the change in the mass of ripple 1 in the first half period. During each half period, the amount of mass transported is small in comparison to the mass of a single ripple. We therefore can neglect changes in the ripple shapes during a half period, and obtain the mass flow during a full period, Δm , by simply adding up the half period mass-flows:

$$\Delta m = \tilde{f}(\lambda_1) - \tilde{f}(\lambda_2). \quad (6)$$

Clearly (6) can be extended to an arbitrary number of ripples. In that case the mass-flow to ripple i , Δm_i , is due to interactions with both ripple $i-1$ and $i+1$: $\Delta m_i = 2\tilde{f}(\lambda_i) - \tilde{f}(\lambda_{i+1}) - \tilde{f}(\lambda_{i-1})$.

To close the equations we need to relate the mass flow to a change in the size of the ripples that exchange the mass. Since the mass-flow is small, it is reasonable to assume that the change in ripple size is linear in the mass transport. The greatest simplification is obtained if we assume all ripples to be of near equal size, so that the ratio $\Delta m / \Delta \lambda$ is equal for all ripples. Taking the continuum time limit and rescaling time to absorb a proportionality constant we obtain:

$$d\lambda_i/dt = -\tilde{f}(\lambda_{i-1}) + 2\tilde{f}(\lambda_i) - \tilde{f}(\lambda_{i+1}). \quad (7)$$

The total length of a system of ripples evolving according to Eq. (7) is conserved. While this model is a bit crude, and we will use a slightly more advanced model in our studies presented in section III C, it nevertheless illustrates the basic consequences of the mass flow for the ripple patterns.

1. Equilibria and stability

The model described by Eq. (7) has two obvious types of equilibria. First of all, the homogeneous situation where all λ 's are equal is an equilibrium state. Secondly,

there are “period two” states, for which $\tilde{f}(\lambda_i) = \tilde{f}(\lambda_{i+1})$ but $\lambda_i \neq \lambda_{i+1}$ (see Fig. 16 in [10] for similar states). In fact, an abundance of more complicated equilibria can be constructed by arbitrary juxtapositions of ripples of lengths λ_a or λ_b when $\tilde{f}(\lambda_a) = \tilde{f}(\lambda_b)$.

The stability of the homogeneous equilibria can easily be determined: linearizing Eq. (7) around its equilibrium state, by setting $\lambda_i = \lambda_{eq} + \delta_i$, we obtain the following equation:

$$d\delta_i/dt = -\tilde{f}'(\lambda_{eq})(\delta_{i-1} - 2\delta_i + \delta_{i+1}) \quad (8)$$

in which we immediately recognize the linear stability equation one obtains for the space-discretized diffusion equation, with diffusion coefficient $-\tilde{f}'(\lambda_{eq})$. Clearly the sign of \tilde{f}' will be the important quantity.

The mass transport that we obtained in section II B 2 has a single maximum at λ_{min} . Therefore, when λ_{eq} is larger than λ_{min} , $-\tilde{f}'(\lambda_{eq})$ is positive and the pattern is stable, while for λ_{eq} smaller than λ_{min} the pattern is unstable and a *short wavelength instability* occurs. Therefore we refer to the value of λ where \tilde{f} is maximal as λ_{min} . These stability properties have a clear interpretation; if we inspect two unequal adjacent ripples with sizes larger than λ_{min} we obtain from Eq. (6) that mass will flow from the larger to the smaller ripple, hence leading to a stable equilibrium. In the opposite case of two unequal adjacent ripples with sizes smaller than λ_{min} mass flows from the smaller to the bigger ripple, which eventually leads to the annihilation of the smaller ripple. Only patterns with $\lambda > \lambda_{min}$ can be stable.

There is however an additional instability for *large* ripples, related to the creation of new ripples, that have been observed in experiments [28,4] and also in our numerical studies [21]. The physical mechanism for this instability follows from the separation bubble dynamics. Once the size of this bubble is smaller than the ripple (see $\lambda=2.0$ in Fig. 3), the mass transport will create inhomogeneities at the lower edge of the ripples, and typically we find that new ripples are created from this. For marginally large ripples this creation will occur in the trough between two large ripples. Something similar happens in the model when we assume that \tilde{f} is defined for arbitrary small values of λ . Suppose we have a homogeneous ripple pattern, such that $\tilde{f}(\lambda_{eq}) < \tilde{f}(0)$. This means that when infinitesimal ripples are inserted in between the large ripples, they will gain mass from the larger ripples. Therefore the large wavelength ripples are also unstable, and we have found the maximum value λ_{max} where homogeneous patterns are stable, i.e., where $\tilde{f}(\lambda_{max}) = \tilde{f}(0)$. It is somewhat surprising that our model captured this instability, since for patterns with infinitesimal ripples the assumption of only nearest neighbor interactions is clearly invalid.

The period-two and more complicated equilibrium states, can be shown to be unstable in our framework; there is experimental evidence that such period-two states can become stable [10] in some parameter regime.

In conclusion: the maximum of the mass exchange between adjacent ripples as a function of their lengths leads, under some mild assumptions, to a number of important qualitative conclusions. Ripples that are either too large or too small are unstable to a *short* wavelength instability.

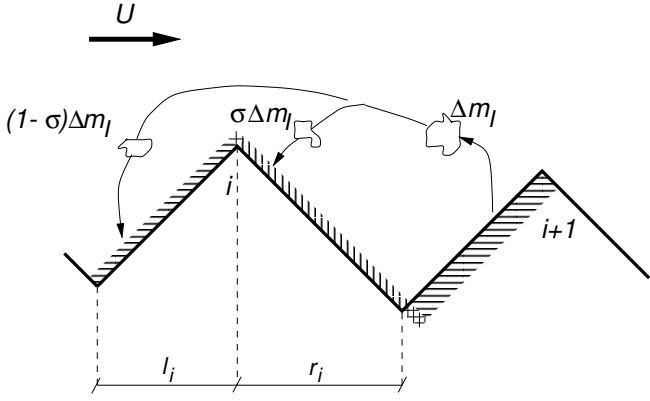


FIG. 6. A sketch of the ripple profile with the triangular ripples and the quantities used to describe the ripples. Note that the ripples do not need to be symmetric. Also shown is the exchange of sediment from the right ripple to the left ripple during the first half wave period.

B. Formulation of a more refined model

The model studied in the previous section, although instructive, is a bit crude. Here we will formulate a more refined model, which no longer requires that all ripples are of near equal size. As before, this model is based on the mass flow between adjacent ripples, but allows for asymmetric ripples: in both our numerical studies and experiments [9] one observes that the ripples are asymmetric during their evolution (although, on average, they are not). The ripples are therefore characterized by two coordinates, being the length of their left and their right sides (see Fig. 6). We denote these lengths by l_i and r_i , and obviously have $\lambda_i = l_i + r_i$. This refinement allows us to let the separation bubbles take mass only from one side of a ripple.

As before, we have to determine how the mass flow depends on these lengths (section III B 1), and how these lengths change due to the mass flow (section III B 2). Conservation of the total length of the ripples and their total mass will lead to a unique set of equations.

1. The mass-flow

Again we will assume that the size of a separation bubble only depend on the length of the lee side of the ripple that generates it. During the first half period the separation bubble transports Δm_I mass from the left slope of

ripple $i + 1$ to ripple i (see Fig. 6). This mass is divided over the left and right slopes of ripple i , with a ratio given by a parameter σ . We have not studied this parameter in detail, but have found that in the full numerical simulations discussed in section II B that σ is not close to 0 or 1. In the numerics presented below, it is set to 0.5.

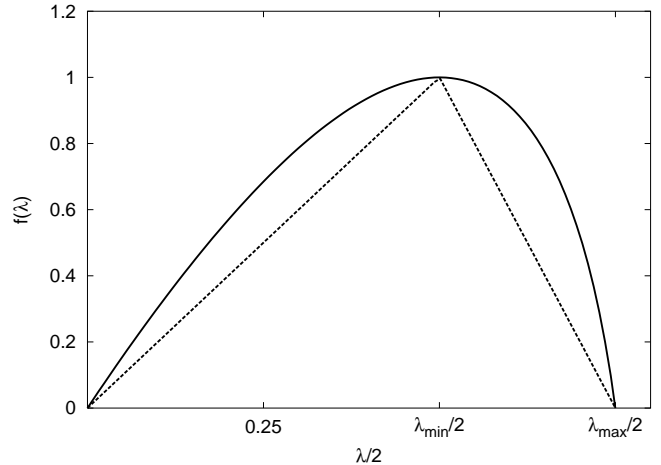


FIG. 7. The interaction functions used in the models. Smooth function, Eq. (13) (full line) and the bi-linear function Eq.(12) (broken line), both shown for a value of $\lambda_{max} = 1.5$.

Since we now will phrase all our dynamics in terms of the left and right slopes of the ripples, we will use the function f instead of \tilde{f} ; remember that f is defined via $f(z) = \tilde{f}(2z)$.

With the masses of the left and right slopes of the ripples being denoted by m_l and m_r , the mass flow in the first half period is:

$$\begin{aligned}\Delta m_{li} &= -f(r_{i-1}) + (1 - \sigma)f(r_i) \\ \Delta m_{ri} &= \sigma f(r_i) .\end{aligned}\quad (9)$$

The mass-flow in the second half period follows by symmetry:

$$\begin{aligned}\Delta m_{li} &= \sigma f(l_i) \\ \Delta m_{ri} &= -f(l_{i+1}) + (1 - \sigma)f(l_i) .\end{aligned}\quad (10)$$

Now we again assume that the mass-transport is small, so we can neglect the changes of the ripple sizes during one half cycle. Adding the contributions from Eqs. (9) and (10) up we obtain for ripple i :

$$\begin{aligned}\Delta m_{ri} &= \sigma f(r_i) + (1 - \sigma)f(l_i) - f(l_{i+1}) \\ \Delta m_{li} &= \sigma f(l_i) + (1 - \sigma)f(r_i) - f(r_{i-1}) .\end{aligned}\quad (11)$$

In our models two different forms for the mass transport function $f(z)$ where used. Both functions have a maximum at $z = 1/2$ and are zero at 0 and $\lambda_{max}/2$ (Fig. 7). The simplest function that satisfies these requirements is bi-linear:

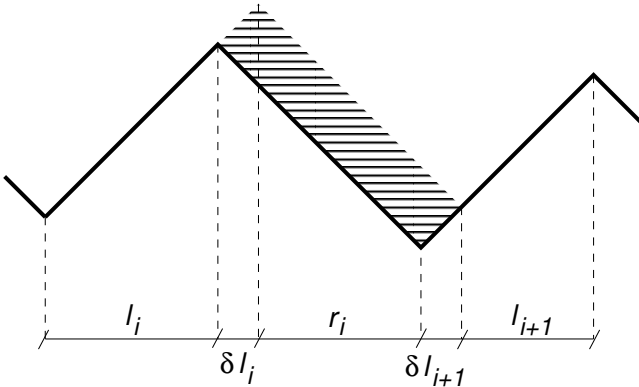


FIG. 8. An illustration of the placement of a mass on the right side of a ripple. This mass introduces a shift in the position of r_i , and consequently a change in the lengths l_i and l_{i+1} . The positions of the trough to the left and the crest to the right are unaffected.

$$f(z) = \begin{cases} 2z & \text{for } z < \frac{1}{2} \\ \left(1 - \frac{2z-1}{\lambda_{max}-1}\right) & \text{for } z \geq \frac{1}{2} \end{cases} . \quad (12)$$

To obtain a smooth function with a quadratic maximum that satisfies $f(0) = f(\lambda_{max}/2) = 0$ we constructed f as the sum of a linear function and a square root:

$$f(z) = \frac{4z}{2 - \lambda_{max}} + \frac{\lambda_{max}(\lambda_{max} - 4)}{2(\lambda_{max} - 2)^2} + \frac{\lambda_{max}}{2(\lambda_{max} - 2)^2} \sqrt{16(\lambda_{max} - 2)z + (\lambda_{max} - 4)^2} . \quad (13)$$

This function is well-defined for λ_{max} between $4/3$ and 4 .

2. Mapping Δm to changes in l and r .

To obtain a closed set of dynamical equations we have to supplement the expressions (11) for the mass-flow as a function of the lengths l_i and r_i by expressions that establish how these lengths evolve under a certain mass flow. Considerations on the conservation of the length and mass and locality yield a unique solution to this problem.

Suppose we have an amount of mass being deposited on the right slope of ripple i only, as sketched in Fig. 8. Due to locality we require that at only the lengths l_i , r_i and l_{i+1} may be affected by this mass-flow. Since we wish to keep the total length of the ripple pattern constant, we require $\delta(l_i + r_i + l_{i+1}) = 0$. On the other hand, the slopes of the ripples are assumed to be at a constant angle, and so $(l_i - r_i + l_{i+1})$ constitutes the height-difference between the trough between ripple i and $i-1$ and the peak of ripple $i+1$ (see Fig. 8). Again, since the ripple pattern away from where the mass transport occurs should be unaffected, we find that $\delta(l_i - r_i + l_{i+1}) = 0$. Combining these two constraints we obtain that a mass flow towards

the right slope of ripple i should *not* change the length r_i .

The only consistent way of changing the lengths is by “shifting” the location of the right slope to the right over a distance Δx , and to deposit all the mass there. This yields for the changes in l :

$$l_i \rightarrow l_i + \Delta x \\ l_{i+1} \rightarrow l_{i+1} - \Delta x , \quad (14)$$

Assuming for simplicity the angle of repose to be 45° , we can calculate the volume of the slab of deposited sand (see Fig. 8) and find that the change in the lengths Δx is given by:

$$\Delta x = \Delta m_{ri} / (2r_i) . \quad (15)$$

To implement such dynamics for the general case where mass transport to and from all slopes takes place one should proceed carefully, since operations as given by Eqs. (14) and (15) do not commute when mass-flows to and from both left and right slopes are considered. To overcome this problem one simply removes and deposits mass in subsequent stages. Denoting the total mass that is to be removed from the left slopes of all the ripples during the first half period by $\Delta m_i = f(r_{i-1})$ this yields the following procedure.

1. Remove from the left slopes the mass that is to be deposited on the right slopes, i.e., $\sigma \Delta m_i$. Update the lengths of all the right sides according to:

$$r_{i-1} \rightarrow r_{i-1} + \frac{\sigma \Delta m_i}{2l_i} - \frac{\sigma \Delta m_{i-1}}{2l_{i-1}} . \quad (16)$$

2. Deposit the masses $\sigma \Delta m_i$ on the right side of ripples $i-1$, and update the left lengths:

$$l_{i-1} \rightarrow l_{i-1} + \frac{\sigma \Delta m_i}{2r_{i-1}} - \frac{\sigma \Delta m_{i-1}}{2r_{i-2}} . \quad (17)$$

3. Now remove from the left slopes the mass which goes to the left sides: $\Delta m_i = (1 - \sigma) \Delta m_i$, and redistribute this mass over the left slopes by updating the length of the right slopes as in Eq. (16).

For the second period of the driving this procedure is repeated for the mass that is taken from the right slopes.

The amount of mass exchanged during one half period is small, and a much simpler dynamics can be implemented which, however, only approximates mass conservation. Ignoring higher order effects and using (14) and (15) we write the total change in the lengths as a function of the changes in the masses then as:

$$\Delta r_i = -\frac{\Delta m_{li+1}}{2l_{i+1}} + \frac{\Delta m_{li}}{2l_i} \\ \Delta l_i = \frac{\Delta m_{ri}}{2r_i} - \frac{\Delta m_{ri-1}}{2r_{i-1}} . \quad (18)$$

This relation together with the mass flow from (11) defines a simplified model. Here the total length is conserved, but masses associated with the small areas which are cross-hatched in Fig. (6), which are of order of $f(\lambda)^2$ are ignored. In our numerical simulations we use this simplified model, since these second order effects are deemed unimportant. This model has the same linear stability properties as the minimal model defined in Eq. (6).

3. Creation and annihilation

If the length of a ripple becomes small this ripple should be annihilated, and in our numerical code this was done for lengths smaller than some threshold ϵ . As discussed in section III A we also have annihilation of ripples, when the length of the ripples become too large. This is incorporated in the model as a “creation rule” when the space between two ripples is longer than $2\lambda_{max}$. It is important to note that in the simulations described below in section III C the dominant process is coarsening, i.e., for the long time dynamics creation does not play a role.

This concludes our discussion of the definition of the one-dimensional model. We want to stress that changes of the details of the formulation do not alter the qualitative behavior. In section III C below we will discuss the results of numerical studies of this model.

C. Coarsening of fully developed ripples

When, in an experimental situation, ripples grow from a flat bed, initially many small ripples are created. They subsequently coarsen and form a final regular steady state with a well-defined final wavelength (see for example Fig. 1 in [9]). On the other hand, the stability analysis of the previous section shows that a wide range of ripple wave lengths can be linearly stable, namely $\lambda_{min} < \lambda < \lambda_{max}$. An interesting question is if we can expect all of these wavelengths to occur as the final wavelength in an experiment, or if we can expect some sort of dynamical wavenumber selection mechanism to take place.

We will study this question by numerical simulations of the model. Even though our models are developed for near-homogeneous situations, we can ask ourselves what happens when we start out with a (disordered) small wavelength pattern and study the dynamic evolution towards an equilibrium state numerically. An example of such evolution is shown in Fig. 9. A fast coarsening process is seen in the beginning, followed by a slower relaxation towards an equilibrium state. The important dynamical process leading to the equilibrium state is the annihilation of ripples, with each annihilation resulting in a longer average ripple length. After the final annihilation, slow diffusive dynamics sets in.

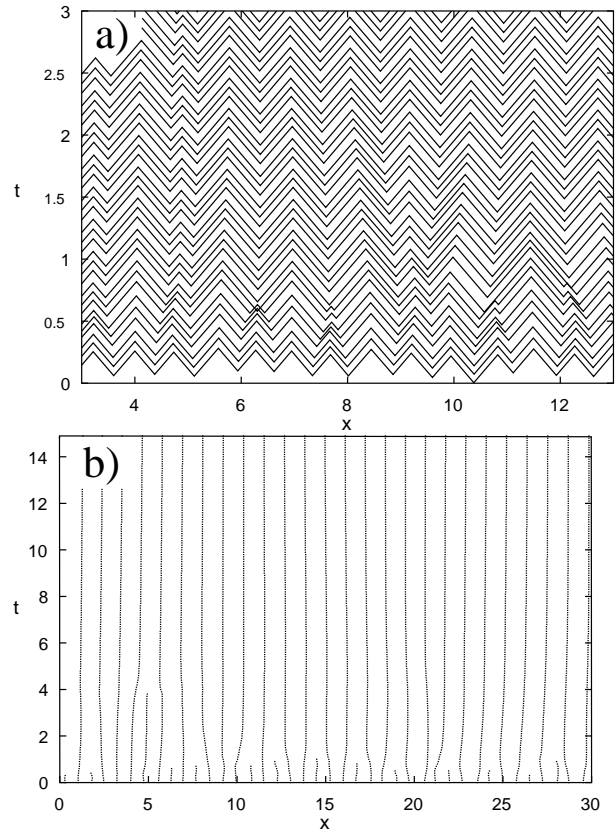


FIG. 9. An example of the dynamics of the model. a) a zoom of the ripple profiles, b) the evolution of the ripple crests. The time scale is arbitrary ($\lambda_{max} = 1.35$).

We assume periodic boundary conditions in our models. The parameters entering the model are the length of the domain L , the parameter σ and the maximum ripple length λ_{max} . The initial conditions are disordered ripples with an average wavelength $\lambda_0 < \lambda_{min}$. One might have expected that the final equilibrium wavelength λ_{eq} could be able to take almost any values in the stable band $\lambda_{min} < \lambda_{eq} < \lambda_{max}$, however the final wavelength turned out to be quite independent upon both the initial average wavelength (λ_0) (when this was sufficiently small) and the initial degree of disorder. Also the value of σ turned out to be of very little importance, as long as it did not come close to the extreme values 0 and 1. This independence of λ_{eq} on the initial conditions is a quite surprising result, which could not have been predicted *a priori* from the model.

The final wavelength does however depend on the shape of the interaction function and the value of λ_{max} . In Fig. 10 λ_{eq} is plotted as a function of λ_{max} for the two proposed interaction functions (12) and (13). The value of σ has been set to 0.5. The final wavelength appears to be a nontrivial function of λ_{max} for both interaction functions. The interaction function which resembles the one from the numerical flow calculations (Fig. 4) is the smooth function with $\lambda_{max} \approx 1.6$. From Fig. 10, this results in an equilibrium wavelength of $\lambda_{eq} \approx 1.28 \pm 0.03$,

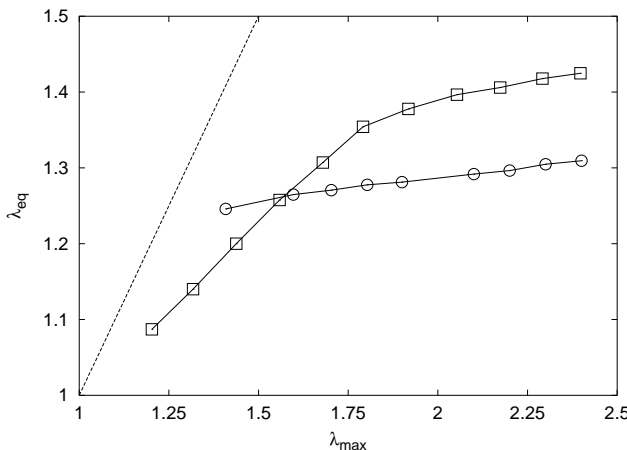


FIG. 10. The equilibrium wavelength as a function of λ_{\max} . The squares correspond to results obtained using the bi-linear interaction function (12), and the circles corresponds to the smooth function (13). The broken line indicates the maximum possible wavelength, $\lambda = \lambda_{\max}$. The initial number of ripples were 1200, and the initial ripple length were 0.7 ± 0.05 .

a result which is in accordance with measured ripple lengths.

To summarize: our simple one-dimensional models are based on symmetry considerations and a mass exchange law that mimics the mass exchange as obtained in detailed modeling of sand ripple formation. Our models display: (i) short wavelength instabilities when the ripples are either to large or too small, (ii) when started from small disordered ripple patterns, coarsening sets in and a rather well-defined final wavelength is found. Finally it should be noted that our models, once the function f is given, predict the dynamics of any initial ripple pattern. More detailed comparisons with experimental data should therefore be made and serve to further validate or falsify our models.

IV. TWO-DIMENSIONAL RIPPLE PATTERNS

Unless one forces the ripple patterns to occur in a narrow channel or annulus, ripple patterns are two-dimensional. The ripples tend to align themselves perpendicular to the anisotropic driving, and so a one-dimensional approximation is a useful first step in their description. However, in particular during the evolution towards the final state, the two-dimensional patterns contain in general many defects [4] which may have an important effect on the wavelength of the final states. To study this we have extended our simple models to two-dimensional patterns.

During the construction of the one-dimensional models we were guided by the full numerical simulations of the flow and mass transport in ripple patterns. We do not have similar simulations for the full three-dimensional

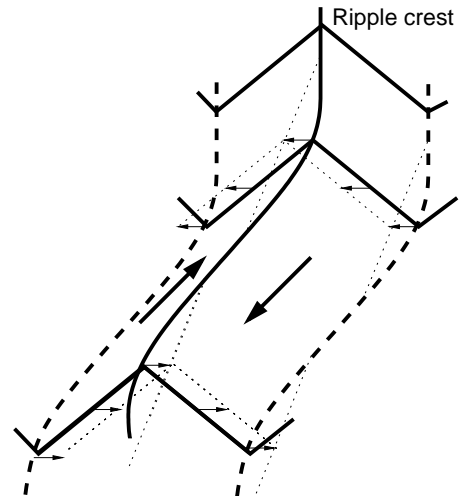


FIG. 11. A sketch of the mass fluxes in the j -direction induced by the crests not being aligned perpendicular to the flow (thick arrows). The mass fluxes induces a movement of the individual ripples and of the crests as a whole.

flow over two-dimensional ripple patterns. We are therefore limited to use general arguments to incorporate the second dimension. The model described below should therefore be considered as a first step in the understanding of full two-dimensional ripple patterns.

Let us denote the direction of the driving by x . The two-dimensional model consists of a large number of one-dimensional models along rows in the x direction which are coupled in the y direction, i.e., along the ridges of the ripples (see Fig. 11). For simplicity we apply periodic boundary conditions in both directions. There are two obstacles to be overcome. First of all we have to determine an expression for the mass flow in the y direction, i.e., mass exchange between neighboring “rows” of ripples. Secondly, we have to decide how to deal with defects, i.e., with the case that two adjacent rows have a different number of ripples.

Our aim is to show how to do this in a physically reasonable way. The model illustrates various scenarios for the dynamics of defects, and shows that the inclusion of defect dynamics alters the “selection” of the final wavelength.

A. Definition

In the two-dimensional setting the individual rows of ripples are similar to those in Fig. 6 and are labeled by an index j , which represents the discrete coordinate in the y -direction. When there are no defects, the ripple at position (i, j) has neighbors at positions $(i, j \pm 1)$ in the y direction and neighbors $(i \pm 1, j)$ in the x direction. As before, the ripples are characterized by their dimensions l_i and r_i , and expression (11) is used to describe the mass flow in the x direction.

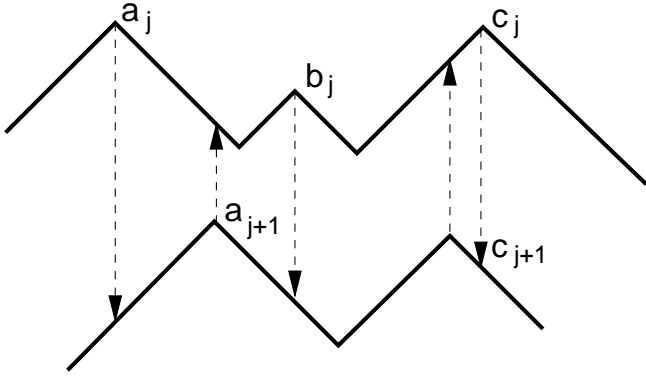


FIG. 12. Illustration of the algorithm used to find neighbors in the y -direction. In this example ripples c_j and c_{j+1} are neighbors. Ripple b_j cannot have a_{j+1} as a neighbor since the neighbor of a_{j+1} is a ; similarly, it can not have c_{j+1} as a neighbor. So ripple b has no neighbor and therefore is a defect.

To describe the mass flow in the y direction, we have to be able to quantify the differences in height between the ripple patterns at j and $j \pm 1$; therefore the height difference between adjacent rows of ripples is an additional degree of freedom. We denote the heights of the crests of the ripples by $h_{i,j}$. Finally, we also need to be able to describe the difference in x -position of crests of ripples in two adjacent rows of ripples j and $(j+1)$; the position of the crest of the i th ripple in the j th row will be denoted by $x_{i,j}$. Notice that since the mass-flows will only depend on differences between positions and heights in adjacent rows, the translational and gauge symmetries are preserved.

a. Mass transport in the y direction We have implemented a mass transport in the y -direction, so that the heights and positions of adjacent rows of ripples tend to equilibrate. Here we do not need to worry about the mass transport in half periods, but instead calculate the transport in the whole wave period.

We will consider the mass transport between ripple (i,j) and $(i,j+1)$ in the situation sketched in Fig. 11; for notational simplicity we will drop the i index here.

The mass flow consists of two parts. The first part is induced by imposing the equivalent of an angle of repose in the y direction, i.e., imposing a certain maximum height difference between h_j and h_{j+1} . The slope in the y direction between these two neighboring ripple crests is just the height difference: $s_{j+\frac{1}{2}} = h_{j+1} - h_j$. If this slope is bigger than the angle of repose, s_c , mass will flow from the higher ripple to the lower ripple:

$$\Delta m_{lj} = \Delta m_{rj} = C_2 \left[s_{j+\frac{1}{2}} H(|s_{j+\frac{1}{2}}| - s_c) - s_{j-\frac{1}{2}} H(|s_{j-\frac{1}{2}}| - s_c) \right], \quad (19)$$

where H is the Heavyside function. This expression leads to a diffusion of the heights, provided that the angle is larger than s_c .

The second part of the mass flow is induced when the ripples are not aligned perpendicular to the main flow. The simplest choice is to assume that this flow is linear in the misalignment of the ripples, i.e., the mass flow between ripple j and $j+1$ is :

$$\Delta m_{rj} = -\Delta m_{lj} = C_1(x_{j+1} - x_j) \quad (20)$$

Such mass-flow leads to a diffusion term in terms of the positions of the ripples. While in principle such behavior would not align ripples which are uniformly slanted, in practise our models are per definition already very anisotropic.

The two expressions (19) and (20) completely specify the mass transport in the y direction between adjacent ripples.

b. Finding neighbors. If there were no defect in the ripple pattern, the determination of the neighbors of ripple (i,j) would be trivial, but due to creation and annihilation of ripples, defects occur. The determination of neighboring ripples in the y -direction is not completely trivial and a specific rule has to be given. Our rule respects two basic principles: *i*) each ripple should have at most one neighbor in each adjacent row, and *ii*) each ripple is its neighbor's neighbor, i.e., if ripple a_{j+1} is ripple a_j 's neighbor, then a_j is the neighbor of a_{j+1} . The implementation of this rule for arbitrary ripple patterns at two adjacent rows is illustrated in Fig. 12. For every ripple crest an imaginary vertical line is drawn to the ripples at the adjacent row. The ripples a_j and a_{j+1} are clearly each other neighbors. The line emanating from crest b_j suggests that b_j is the neighbor of a_{j+1} , but since a_{j+1} is already the neighbor of a_j , we have to conclude that b_j has no neighbors in row $(j+1)$; hence we have detected a defect.

Note that under this rule ripples with the smallest crest to crest distance are not always neighbors; the height of the ripples also plays a role here. For example, in Fig. 12, a_{j+1} 's neighbor is a_j , although the crest of b_j is closer to a_{j+1} than a_j 's crest. Of course, Fig. 12 displays a rather extreme configuration; in the simulations we performed, especially for later times, the ripple ridges are quite vertical and such extreme configurations rarely occur.

Due to the diffusion of the height, a defect can trigger the creation of a new ripple. Suppose ripple (i,j) has no neighbor on row $(j+1)$ such that this ripple is in front of a trough. If the difference of height between (i,j) and the corresponding trough on row $(j+1)$ is larger than s_c , a small ripple is added at the position of the trough on line $(j+1)$. The small amount of mass corresponding to this addition is fixed, it is the same as we use in the creation process for the one-dimensional case, but here we will also remove this mass from the (i,j) ripple. Of course the creation process existing in the one-dimensional case is still active as well.

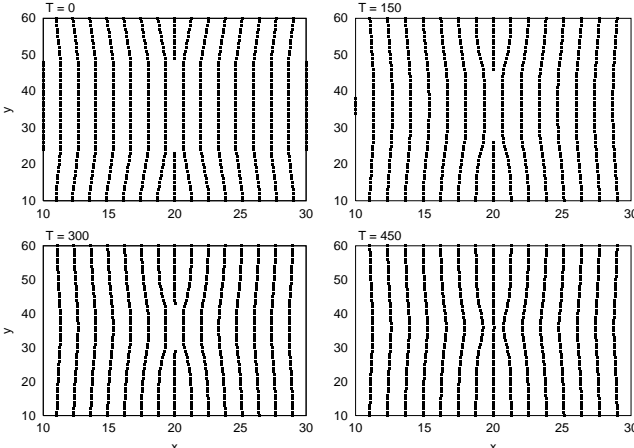


FIG. 13. An example of a climbing defect in a system with 30 ripples in the middle and 31 ripples in the top and the bottom. ($\lambda_1 = 1.29$, $\lambda_2 = 1.33$).

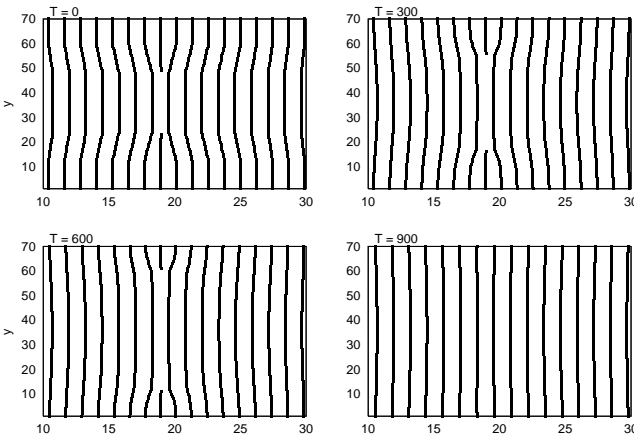


FIG. 14. An example of a de-climbing defect ($\lambda_1 = 1.22$, $\lambda_2 = 1.26$).

B. Numerical results

We have performed numerical studies of the two-dimensional model, using the smooth interaction function, to gain insight in the role of defects. First of all, we studied climbing motion of defects in a small system, consisting of 72 rows with an initial condition of 30 or 31 ripples on each row and two defects, one in the top and one in the bottom of the system (see Figs. 13 and 14). Finally we studied the evolution of a two-dimensional ripple pattern starting from a disordered initial condition and compared it with the one-dimensional case. We have fixed the parameters governing the diffusion in the y -direction to $sc = 0.08$, $C_1 = 0.08$ and $C_2 = 0.02$, and in all cases the smooth interaction function (13) was used. The qualitative results are not sensitive to changes in the values of these parameters.

In the small system we initially have two patches with different wavelength, λ_1 and λ_2 ($\lambda_1 < \lambda_2$) separated by

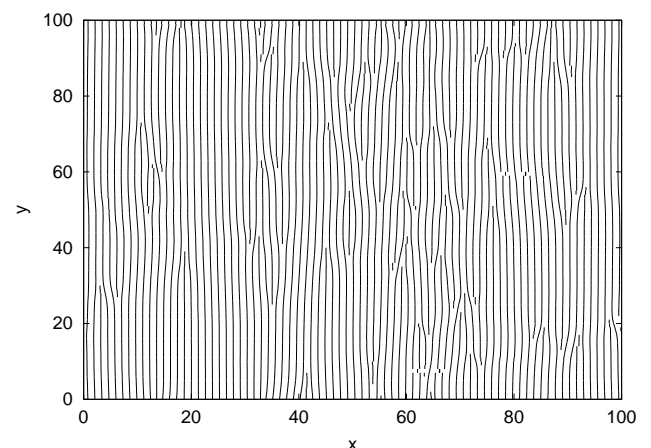


FIG. 15. A snapshot during the evolution of a big system of two-dimensional ripples. The initial conditions were $\lambda_0 = 0.5$. The snapshot is taken after 3200 iterations ($\lambda_{max} = 1.35$, $C_1 = 0.08$, $C_2 = 0.02$).

two defects. In the case where λ_2 is unstable with respect to the defect, the defect will climb into the patch of ripples with length λ_2 (Fig. 13), and the final wavelength becomes λ_1 . In the case where λ_2 is stable with respect to the defect, the defect will de-climb (Fig. 14), and the final wavelength is λ_2 . The wavelength where there is a cross-over between climbing and de-climbing gives the marginal wavelength for stability with respect to climbing and de-climbing defects, λ_{def} . When one moves very close to the marginal wavelength the speed of the dynamics slow down, and due to the inherent thresholds for creation/annihilation in the implementation of the model, eventually the defects stops moving. This makes it hard to estimate the value of λ_{def} accurately. For a system with 30 (31) ripples we find $\lambda_{def} = 1.28 \pm 0.03$.

Both here and in the one-dimensional system ripples with lengths longer than 1 are stable. When defects

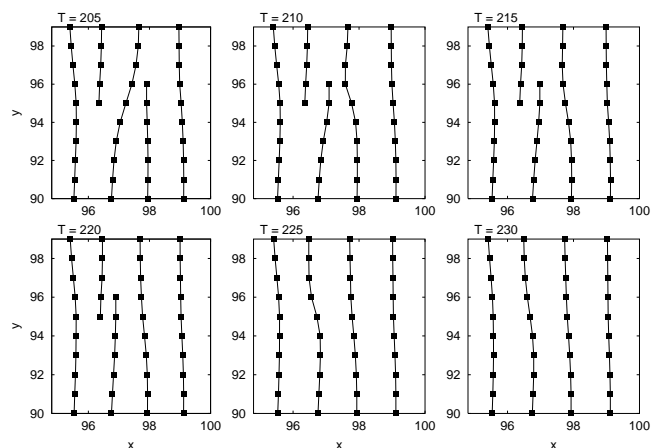


FIG. 16. An example of the annihilation of two defects by reconnection.

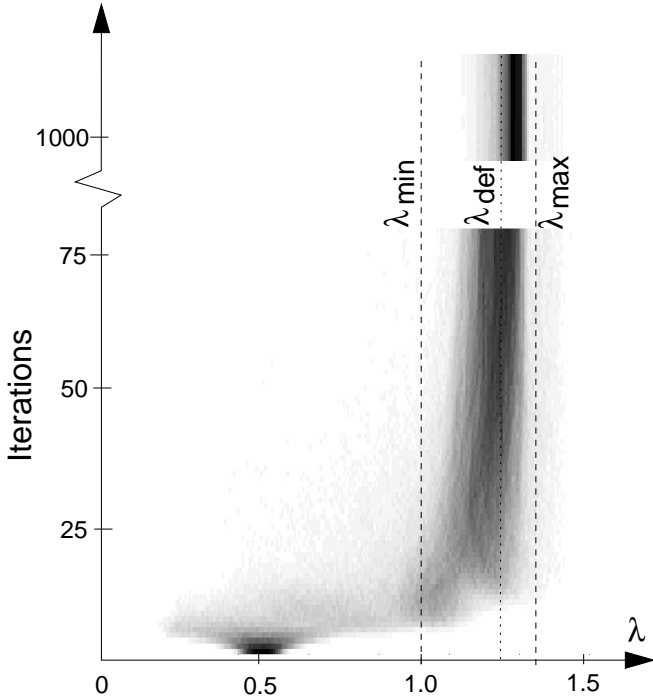


FIG. 17. Evolution of the wavelength distribution with time in the large system, with black being the most probable wavelength.

are present, only states with wavelengths larger than ~ 1.28 survive. We can therefore expect the final wavelength λ_{eq} in a two-dimensional system to be larger than in a one-dimensional system, and it should lie between λ_{def} and λ_{max} .

To check this prediction we have performed simulations in a large systems of between 100 and 200 ripples and 100 rows (Fig. 15). The initial conditions were ripples of length $\lambda_0 = 0.5$. As in the small system, climbing and de-climbing of defects occur, but one also observes the annihilation of defects due to reconnections similar to Fig. 16. Similar to the one-dimensional model and the experiments we find that the system evolves very rapidly via coarsening to a state with a low density of defects. After this initial disordered transient, which last for approximately 100 periods, the dynamics slows down dramatically. This is illustrated on Fig. 17, where we have represented the evolution of the wavelength distribution as a function of time. Even after thousands periods there are still persistent defects, and so the distribution of the wavelengths is not sharp. The peak of the distribution clearly lies in between λ_{def} and λ_{max} .

Runs with the two-dimensional model with different values of λ_{max} show that the equilibrium wavelength is systematically larger than in the one-dimensional case (see Fig. 18).

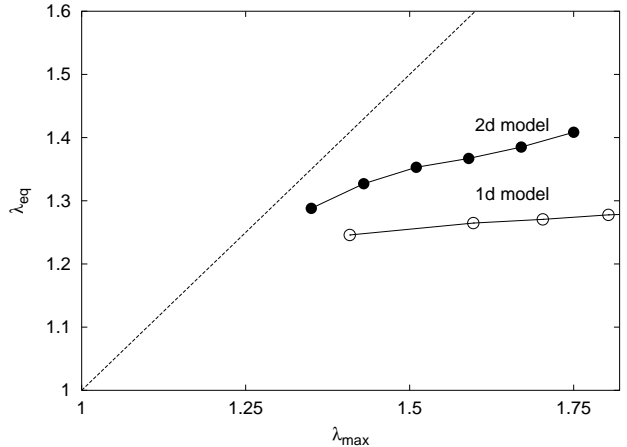


FIG. 18. The final wavelength in the two-dimensional case compared with the results for the one-dimensional case. The straight line is $\lambda_{eq} = \lambda_{max}$.

V. DISCUSSION AND CONCLUSION

We have constructed a number of simple models to describe the dynamics of fully developed vortex ripples. These models are not based on an expansion around the flat bed state, but on the exchange of mass between fully developed ripples.

To study the behavior of these models, generic forms of the mass-transfer function were used. The precise form of this mass transport can be determined from advanced numerical modeling of the sand-water dynamics for fully developed ripples or from experiments. With an accurate form of the mass-transfer function it is possible, in principle, to use these models for quantitative predictions of the dynamics of near-equilibrium patterns, the wavelength of fully developed ripples in the final state and the timescale of the development of ripple patterns.

The models have been used to study the coarsening process of the ripples numerically. It was found that as long as the initial ripple length was sufficiently smaller than the marginal length λ_{min} , a unique ripple length was found after the coarsening. The dynamics leading to the final wavelength is strongly influenced by the annihilation of individual ripples, which makes it hard to find an analytical estimate of the final wavelength.

The secondary instabilities that fully developed ripple patterns can suffer when the driving amplitude a is suddenly changed were predicted to be of short wavelength nature. Experiments on two-dimensional sand patterns performed in Copenhagen [4] are consistent with this prediction, although in some case fully two-dimensional modulations of the basic ripple state appear to occur.

Since our two-dimensional model only assumes diffusion-like dynamics in the y -direction we should not be surprised that not all details of the full experimental situation are captured. However, our model predicts that

the presence of defects leads to a narrowing of the band of stable ripples. The narrowing results in a final state with longer ripples than in the one-dimensional model. This results indicates that one should be careful when results from experiments with one-dimensional ripples are generalized to ripples in Nature.

In conclusion: vortex ripple pattern formation combines a number of features, of which the most important are: (i) a strongly anisotropic driving (ii) no intrinsic length-scale for patterns, but a scale set by the driving (iii) the initial bifurcation is strongly subcritical (iv) patterns can experience short wavelength instabilities. We

have presented here simple models that capture important aspects of this unique pattern forming system.

VI. ACKNOWLEDGMENTS

It is a pleasure to acknowledge discussions with Markus Abel, Tomas Bohr, Jørgen Fredsøe, Jonas Lundbek Hansen and Alexandre Stegner. M.v.H. acknowledges financial support from the EU under contract ERBFMBICT 972554. M.-L.C. thanks the Niels Bohr Institute for hospitality.

[1] R. A. Bagnold, *The Physics of blown sand and desert dunes*, Chapman and Hall, Methuen, London, (1941).

[2] A. J. Raudkivi, J. of Hydraulic Eng., 58–64 (1997).

[3] R. A. Bagnold, Proc. Roy. Soc. London A, **187**, 1–15, (1946).

[4] K. H. Andersen, T. Bohr, C. Ellegaard, A. Haaning, J. L. Hansen, T. Sams and M. van Hecke, in preparation.

[5] K. H. Andersen, preprint, arXiv:nlin.PS/9909006 (1999).

[6] H. Nishimori, M. Yamasaki and K. H. Andersen. Int. J. of Mod. Phys. B **12**, 257–272 (1998).

[7] E. A. Hansen, J. Fredsøe, and R. Deigaard, J. of Waterway, Port and Ocean Engineering, **120**, 37 (1994).

[8] J. Fredsøe, K. H. Andersen and M. Sumer, Coastal Engineering 38, 177–221 (1999).

[9] A. Stegner and J. E. Wesfreid, Phys. Rev. E **60**, R3487 (1999).

[10] M. A. Scherer, F. Melo and M. Marder, Phys. of Fluids **11**, 58 (1999).

[11] R.A. Anderson, Earth-Science Reviews, **29**, 77–96 (1990).

[12] H. Nishimori and N. Ouchi. Phys. Rev. Lett. **71**, 197 (1993).

[13] L. Prigozhin, preprint, cond-mat/9807006 (1998).

[14] O. Terzidis, P. Claudin and J.-P. Bouchaud, The European Physical Journal, **5**, 245–249 (1998).

[15] Z. Csahók, C. Misbah, F. and A. Valance, Physica D, **128**, 87–100 (1999).

[16] A. Betat, V. Frette and I. Rehberg, Phys. Rev. Lett. **83**, 88–91 (1999).

[17] M. C. Cross and P. C. Hohenberg. Rev. of Mod. Phys., **65**, 854 (1993).

[18] P. Blondeaux. J. Fluid Mech., **218**, 1 (1990).

[19] P. Blondeaux and G. Vittori, J. Fluid Mech. **226**, 257 (1991).

[20] G. Vittori and P. Blondeaux. J. Fluid Mech. **239**, 23, (1991).

[21] K. H. Andersen, *Ripples beneath surface waves and topics in shell models of turbulence*, PhD thesis Copenhagen University (unpublished); <http://www.nbi.dk/~kenand/Thesis.html>, (1999).

[22] K. H. Andersen and J. Fredsøe, in preparation, (2000).

[23] H. Ayrton, Proc. Roy. Soc. London A, **84**, 285, (1910).

[24] J. R. Dingler, PhD thesis, University of California, (unpublished) (1975).

[25] P. Nielsen, J. of Geophysical Research **86**(C7), 6467 (1981).

[26] P. L. Wiberg and C. K. Harris, J. of Geophysical Research, **99**(C1), 775 (1994).

[27] P. Traykovski, A. E. Hay, J. D. Irish, and J. F. Lynch. J. of Geophysical Research, **104**(C1), 1505 (1999).

[28] K. E. B. Lofquist, in *17.th. Int. Conf. on Coastal Engineering in Sydney, Australia*, volume 3, 3087 (1980).

[29] J. F. A. Sleath, Continental Shelf Research, **1**(1), 33 (1982).

[30] P. P. Mathisen and O. S. Madsen, J. of Geophysical Research **101**(C7), 16533 (1996).

[31] K. H. Andersen and M. Lohmann, Int. Conf. Coastal Eng., Sydney (2000).

[32] J. Fredsøe and I. Brøker, Progress Reports from ISVA, the Danish Technical University, **58**, 19 (1983).

[33] D. C. Wilcox, AIAA Journal **26**, 1299 (1988).

[34] J. Fredsøe and R. Deigaard, *Mechanics of coastal sediment transport*, World Scientific, (1992).

[35] E. Meyer-Peter and R. Müller, in *Second meeting, Stockholm, Int. Ass. for Hyd. Structures Res.*, 39 (1948).

[36] F. Engelund and J. Fredsøe, Nordic Hydrology, **7**, 293 (1976).

[37] A. Kovacs and G. Parker, J. Fluid Mech., **267**, 153–183 (1994).